ACS NANO

www.acsnano.org

ARTICLE

Interstitially Bridged van der Waals Interface Enabling Stacking-Fault-Free, Layer-by-Layer Epitaxy

GunWoo Yoo,[▽] TaeJoon Mo,[▽] Yong-Sung Kim,* Chang-Won Choi, Gunho Moon, Sumin Lee, Chan-Cuk Hwang, Woo-Ju Lee, Min-Yeong Choi, Jongyun Choi, Si-Young Choi,* Moon-Ho Jo,* and Cheol-Joo Kim*

Cite This: https://doi.org/10.1021/acsnano.5c07577

Read Online

ACCESS | Metrics & More | Article Recommendations | Supporting Information

ABSTRACT: van der Waals (vdW) crystals are prone to twisting, sliding, and buckling due to inherently weak interlayer interactions. While thickness-controlled vdW structures have attracted considerable attention as ultrathin semiconducting channels, the deterministic synthesis of stacking-fault-free multilayers remains a persistent challenge. Here, we report the epitaxial growth of single-crystalline hexagonal bilayer MoS_2, enabled by the incorporation of Mo interstitials between layers during layer-by-layer deposition. The resulting bilayers exhibit exceptional structural robustness, maintaining their crystallinity and suppressing both rotational and translational interlayer misalignments even after transfer processes. Atomic-resolution analysis reveals that the Mo interstitials are located at a single sublattice site within the hexagonal lattice, where they form tetrahedral bonds with sulfur atoms from both MoS_2 layers, effectively anchoring the interlayer registry. Density functional theory calculations further indicate that these Mo atoms act as nucleation centers, promoting the selective formation of the hexagonal bilayer phase. This approach offers a robust strategy for the deterministic growth of multilayer vdW crystals with precisely controlled stacking order and enhanced interlayer coupling.

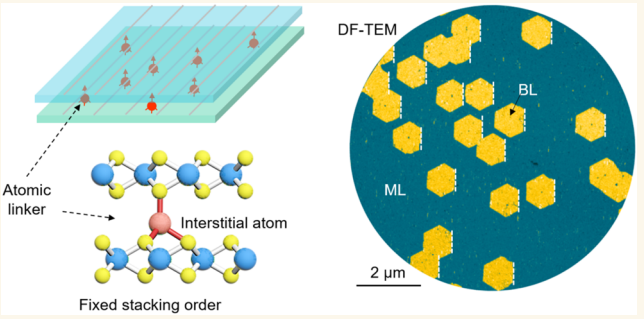

KEYWORDS: *van der Waals materials, layer-by-layer epitaxy, stacking-fault-free, interstitials, interlayer covalent bridging*

Deterministic growth of single-phase layered materials is essential for realizing phase-sensitive properties with uniformity and scalability. While thickness-controlled van der Waals (vdW) structures have garnered significant interest as ultrathin semiconducting channels[1,2] many layered compounds can adopt multiple polytypes through variations in interlayer stacking sequences, leading to distinct crystal symmetries and emergent physical properties.[3,4] Parameters such as temperature,[5−7] pressure[8−10] and chemical environment[11−13] can thermodynamically bias the formation of specific polymorphs within a given phase diagram. However, the free energy differences between stable vdW polytypes—typically on the order of a few meV per unit cell—are exceedingly small due to weak interlayer interactions, making precise phase selection intrinsically challenging (see Figure 1a for a schematic of bilayer transition metal dichalcogenides).[14−16]

Recent advances have demonstrated the controlled synthesis of multilayer transition metal dichalcogenides (TMDs) with rhombohedral stacking order, achieved via edge-assisted nucleation[17] and interfacial epitaxy.[18] These approaches leverage stronger interfacial interactions—on the order of ∼100 meV per unit cell—between the TMDs and substrate step edges to stabilize a specific stacking configuration. Yet, the weak intrinsic interlayer bonding remains insufficient to resist shear or tensile deformation, leading to postgrowth stacking variations such as phase coexistence with opposite out-of-plane polarities[19,20] and the formation of strained solitons.[21−23] This underscores the continued difficulty in achieving structurally robust, single-phase multilayers with deterministically engineered stacking.

Received: May 7, 2025
Revised: July 23, 2025
Accepted: July 23, 2025

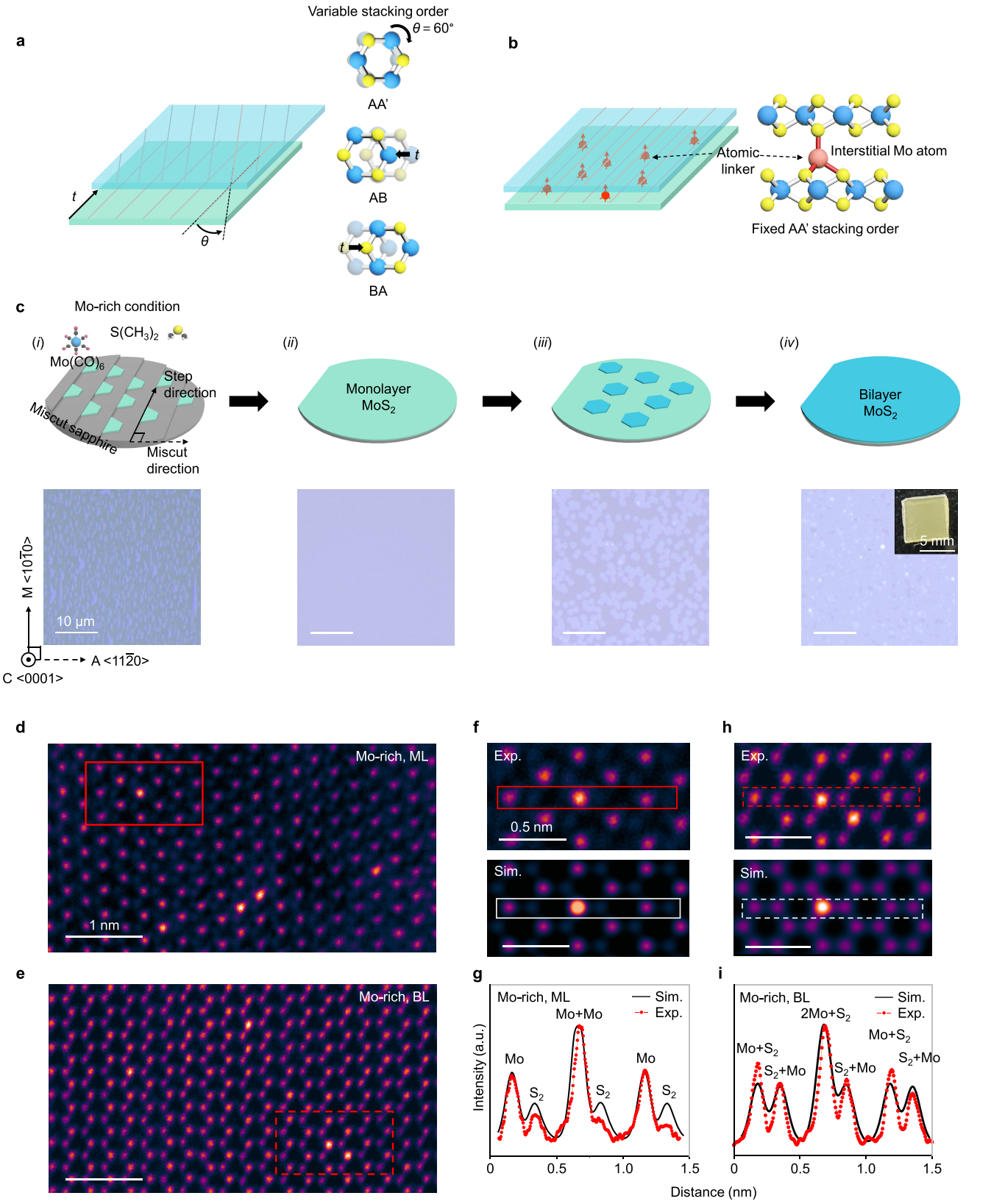

Figure 1. Layer-by-layer epitaxy of MoS_2 with interstitial single Mo atoms. (a) Schematic illustrations of bilayer MoS_2 with various stacking orders induced by layer translation and rotation. (b) Schematic of bilayer MoS_2 incorporating Mo interstitial atoms, which act as atomic linkers covalently connecting adjacent layers. (c) Schematic of the layer-by-layer epitaxy process of bilayer MoS_2 on a miscut sapphire substrate, accompanied by optical reflectance images at each stage. (d), (e) STEM images of monolayer (d) and bilayer (e) MoS_2 grown under Mo-rich conditions. (f) Experimental STEM image from the region highlighted in (d) (top) and a corresponding simulated image of a monolayer containing a Mo adatom located at a Mo lattice site (bottom). (g) Intensity profiles extracted from the boxed region in (f), comparing experimental (red) and simulated (black) data. (h) Experimental STEM image from the region highlighted in (e) (top) and the

https://doi.org/10.1021/acsnano.5c07577
ACS Nano XXXX, XXX, XXX−XXX

Figure 1. continued

corresponding simulated image of a bilayer with a Mo adatom at a Mo site in the lower monolayer (bottom). (i) Intensity profiles extracted from the boxed region in (h), showing experimental (red) and simulated (black) results.

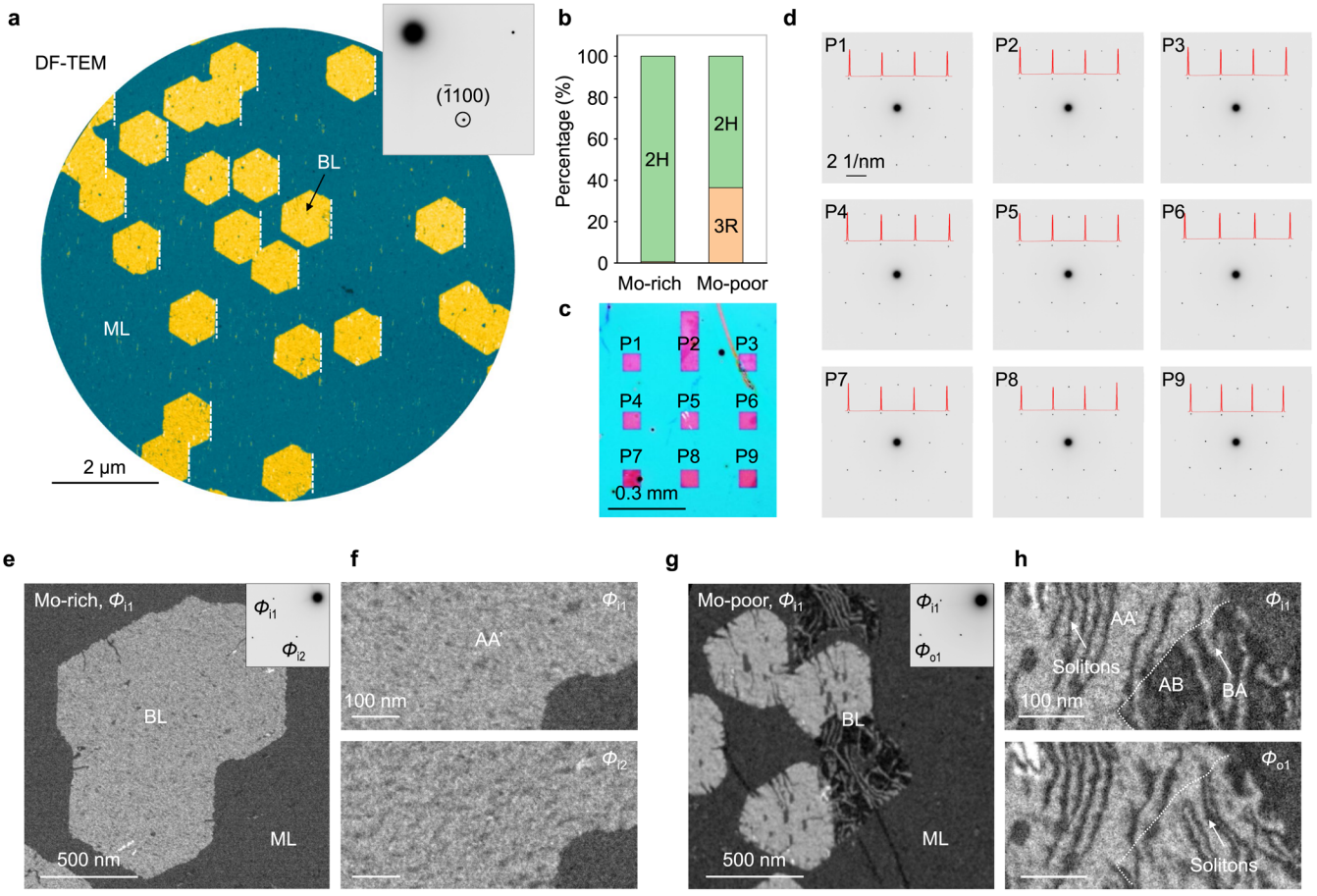

Figure 2. Uniform growth of robust, single-phase bilayer MoS_2 film. (a) DF-TEM image obtained using an inner diffraction spot (upper right). The yellow hexagonal grain corresponds to the bilayer MoS_2 region, while the cyan background indicates the monolayer region. (b) Histogram comparing the bilayer phase distributions grown under Mo-rich and Mo-poor conditions. (c) Optical reflectance image of bilayer MoS_2 grown under Mo-rich conditions and transferred onto a silicon nitride TEM grid. Positions P1−P9 denote suspended regions above the grid windows. (d) Selected-area electron diffraction (SAED) patterns acquired from the positions marked in (c). The red line indicates the intensity profile across the diffraction spots. (e) DF-TEM image of a bilayer grain grown under Mo-rich conditions; the corresponding diffraction pattern is shown in the upper right. (f) DF-TEM images obtained using different diffraction spots from (e). (g) DF-TEM image of bilayer grains grown under Mo-poor conditions; corresponding diffraction pattern shown in the upper right. (h) DF-TEM images obtained using an inner (top) and outer (bottom) diffraction spot.

Interstitial atom engineering has emerged as a promising strategy to overcome this limitation by strengthening interlayer coupling through the deliberate incorporation of atoms into the vdW gap. Theoretical studies suggest that specific transition metal interstitials—such as Mo, W, or Ta—can reside at high-symmetry sites between TMD layers, forming tetrahedral or octahedral covalent bonds with adjacent chalcogen atoms (S, Se, or Te).[24,25] These covalent interlayer bridges can significantly raise the interlayer interaction energy—by up to hundreds of meV per unit cell—thereby stabilizing selected stacking configurations (e.g., 2H vs 3R). This enhanced coupling provides a robust thermodynamic driving force for deterministic phase selection during growth.

Experimental realization of such covalently bonded layered materials has been achieved in several systems, most notably in Ta- and V-based TMDs under metal-rich growth conditions.[12] However, for technologically important semiconductors like MoS_2, intercalated phases are theoretically predicted to exhibit relatively high formation energies, and experimental demonstrations of stacking order control via interstitial incorporation remain limited. Thus, the development of interstitial-based strategies tailored for semiconducting TMDs such as MoS_2 represents a critical and largely unexplored frontier in the field.

RESULTS AND DISCUSSION

Layer-by-Layer Epitaxy of Single Crystalline Bilayer MoS_2 Film with Interstitial Mo Atoms. Here, we develop a strategy to incorporate Mo interstitial atoms between layers for single-crystalline bilayer MoS_2 films. These interstitials function as atomic anchors, covalently bridging adjacent layers and promoting the formation of a uniform hexagonal phase with enhanced interlayer coupling (Figure 1b). During layer-by-layer epitaxy, unidirectionally aligned monolayer MoS_2

https://doi.org/10.1021/acsnano.5c07577
ACS Nano XXXX, XXX, XXX−XXX

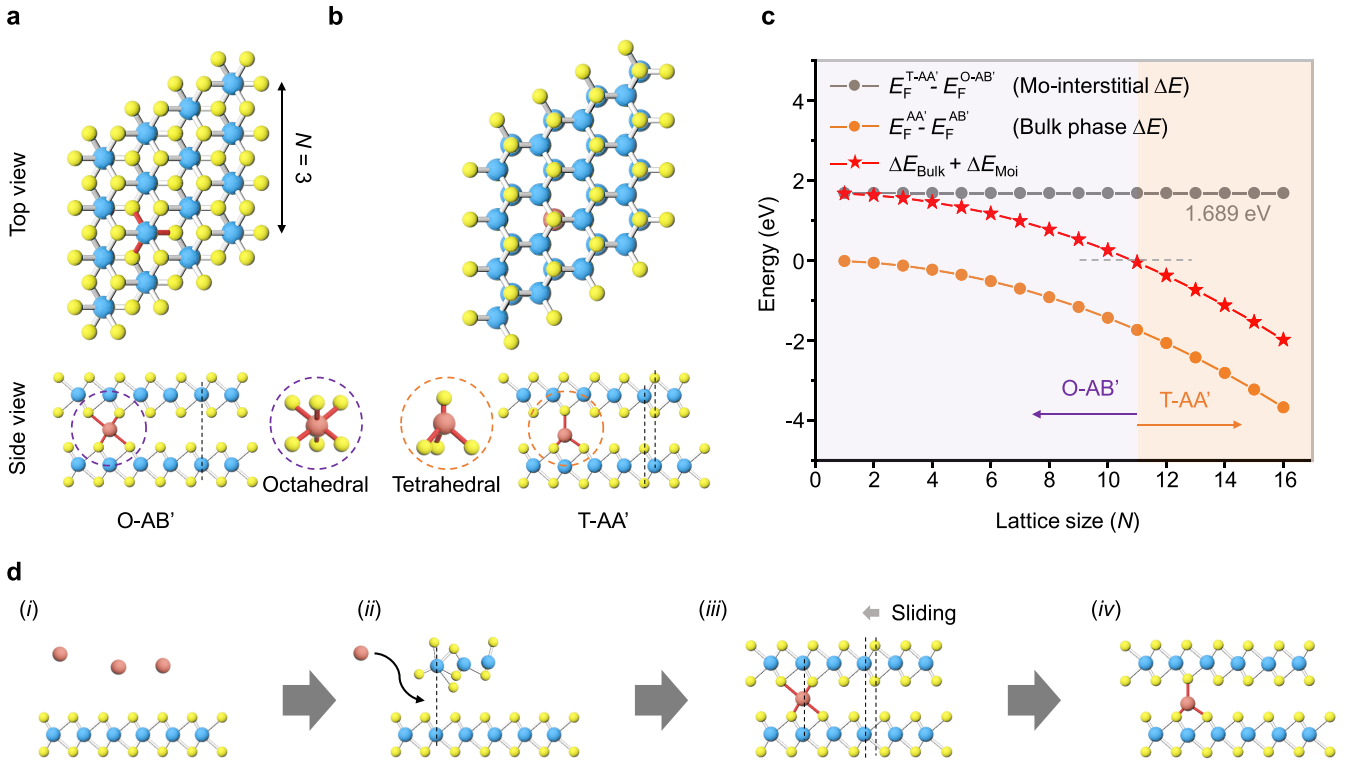

Figure 3. Mechanism of single-adatom-seed-driven epitaxy of hexagonal bilayers. (a), (b) Top and side views of the two most stable atomic configurations of hexagonal bilayer MoS_2 with a Mo interstitial, based on DFT calculations. N denotes the number of MoS_2 unit cells along one axis of the simulation cell. Red spheres indicate Mo interstitials. (c) Formation energy as a function of N. Gray: energy difference of Mo interstitials between T-AA′ and O-AB′ configurations; orange: energy difference between bulk AA′ and AB′ phases; red: total energy difference between T-AA′ and O-AB′, combining interstitial and bulk contributions. (d) Schematic illustration of the proposed layer-by-layer epitaxy mechanism for hexagonal bilayer MoS_2 incorporating a Mo interstitial as a nucleation seed.

grains coalesce into a continuous film on miscut c-plane sapphire via step-directed epitaxy[26] (steps (*i*) and (*ii*) in Figures 1c and S1). Subsequent nucleation of monolayer grains on the first-grown MoS_2 surface leads to the formation of the second layer (steps (*iii*) and (*iv*) in Figures 1c and S2). Notably, the growth was conducted under Mo-rich conditions, using a high-flux Mo supply with a partial vapor pressure ratio between Mo and S precursors, $P_{Mo}/P_S \sim 4 \times 10^{-2}$; See Methods Section. This condition was enabled by the high volatility of the metal−organic chemical vapor deposition (MOCVD) precursors.[27]

High-angle annular dark-field scanning transmission electron microscopy (HAADF-STEM) was used to examine the atomic configurations of the sample grown under Mo-rich conditions (Figure 1d). In the monolayer regions, Mo atoms exhibit strong scattering intensities arranged in a hexagonal lattice, while isolated sites with significantly enhanced intensities are observed. These sites exhibit an area density of 3×10^{13} cm^{-2}, corresponding to approximately one interstitial per ~ 40 MoS_2 unit cells (Figure S3). The intensity profile across these bright atomic sites aligns well with simulation data for a single Mo atom positioned on a Mo lattice site in monolayer MoS_2 (Figure 1f,g). In bilayer regions, similarly bright atomic sites appear (Figure 1e), vertically aligned with Mo sites in the bottom layer (Figure 1h,i), comparable density of 2.4×10^{13} cm^{-2}. In contrast, samples grown under Mo-poor conditions ($P_{Mo}/P_S \sim 2 \times 10^{-3}$; See Methods Section) show negligible evidence of interstitial or adatoms (Figure S4).

We found that growth under Mo-rich conditions are essential for deterministic control of the stacking order. During the second-layer nucleation, Wulff-shaped hexagonal grains form with edges aligned perpendicular to the miscut direction of the sapphire substrate, as indicated by dotted lines in the dark-field transmission electron microscopy (DF-TEM) image (Figure 2a), captured using an objective aperture to collect electrons diffracted by the $(\bar{1}100)$ planes. The bilayer regions exhibit approximately four times the intensity of the monolayer regions, indicating hexagonal stacking order[28,29] (Figure S5). Across the examined sample area, over 99% of bilayer domains (159 out of 160) exhibit hexagonal stacking order (Figure S6), in stark contrast to samples grown under lower Mo concentrations, which show mixed hexagonal and rhombohedral phases (Figures 2b and S7). Continued growth under Mo-rich conditions yields full bilayer coverage (step (iv)) with uniform diffraction patterns (Figure 2c,d), confirming the deterministic formation of hexagonal stacking order.

Remarkably, bilayers grown under Mo-rich conditions maintain a single-phase structure without strained solitons, even after transfer of the samples, as shown in DF-TEM images taken from different diffraction spots (Figure 2e,f). This structural robustness against local variations in stacking order induced by external shear or tensile strains suggests the presence of strong interlayer coupling. In contrast, samples grown under Mo-poor conditions display triangular grains on the first MoS_2 layer, oriented in opposite directions and exhibiting varying intensities in DF-TEM images acquired from an inner diffraction spot—corresponding to the hexagonal and rhombohedral phases, respectively (Figure 2g). Additionally, strained solitons are abundantly observed in both phases in

https://doi.org/10.1021/acsnano.5c07577
ACS Nano XXXX, XXX, XXX−XXX

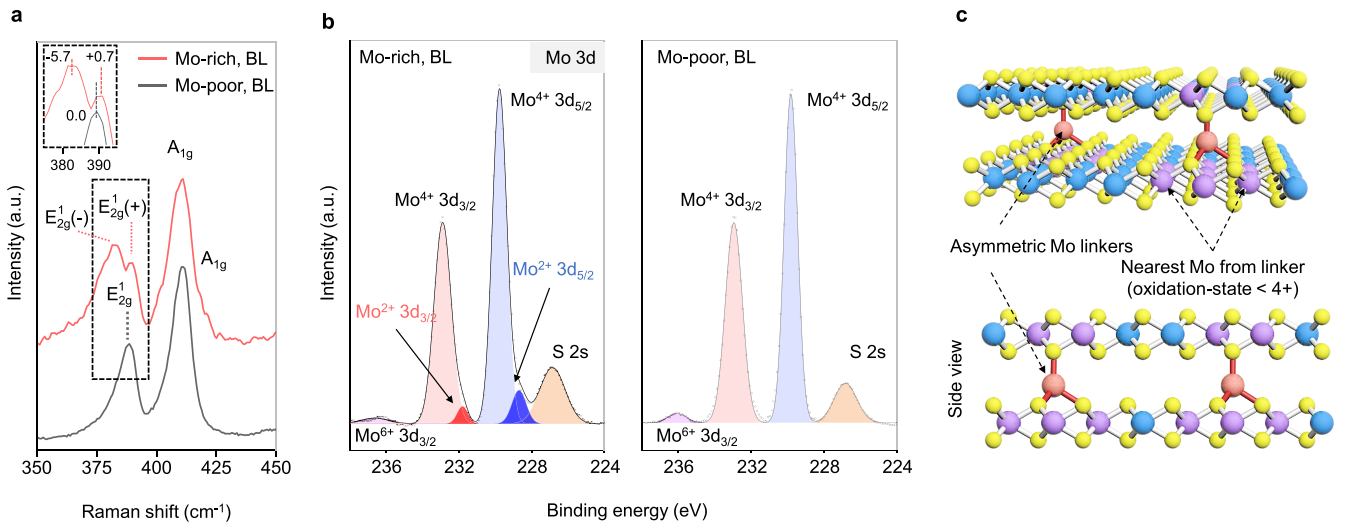

Figure 4. Structural and chemical properties of bilayer MoS_2 with Mo interstitials. (a) Raman spectra of bilayer MoS_2 grown under Mo-rich (red) and Mo-poor (black) conditions. The Mo-rich sample exhibits peak splitting, referenced to the E^1_{2g} mode of the Mo-poor sample (inset). (b) XPS spectra of bilayer MoS_2 grown under Mo-rich (left) and Mo-poor (right) conditions, showing the Mo 3d. S 2p peaks are shown in Figure S10. (c) Schematic illustration of bilayer MoS_2 with a Mo interstitial acting as a linker between layers. Red spheres denote Mo interstitials; purple spheres represent adjacent Mo atoms, whose oxidation states are affected by the nearby interstitials.

DF-TEM images taken from different diffraction spots (Figure 2h), consistent with previous reports.[21,22]

Growth Mechanism of Single-Crystalline Bilayer MoS_2 with Mo Interstitial. To elucidate the mechanism determining the stacking order, we investigated the structural correlations between Mo interstitial atoms and interlayer stacking order using density functional theory (DFT) calculations. The two most stable atomic configurations of bilayer MoS_2 with a Mo interstitial both exhibit hexagonal stacking orders (Figures 3a,b and S8). The lowest formation energy (E_F) is obtained when the Mo interstitial aligns vertically with the Mo atoms in both the top and bottom layers, occupying an octahedral site and forming covalent bonds with neighboring S atoms on each side, resulting in a total coordination number of six within the AB′ stacking configuration (O-AB′; Figure 3a). Within the AA′ stacking configuration, the Mo interstitial can occupy a tetrahedral site, resulting in a total coordination number of four (T-AA′; Figure 3b).

We compare the difference in E_F (ΔE_F) between T-AA′ and O-AB′ stackings as a function of lattice size (N) in the presence of an interstitial atom, as shown in Figure 3c. The formation energies (E_F) of each structure are primarily governed by two contributions: E_{Moi}, representing the formation energy of a Mo interstitial and E_{Bulk}, representing the formation energy of the bulk bilayer. The positive ΔE_{Moi} for a Mo interstitial (gray data) indicates that the O-AB′ stacking is energetically favored over T-AA′ by 1.689 eV per Mo interstitial atom. In contrast, for the bilayer region separated by vdW gaps (orange data), ΔE_{Bulk} becomes negative, indicating that T-AA′ is more favorable than O-AB′; this energy difference increases in magnitude as N increases, corresponding to a larger bilayer area. The total ΔE_F changes sign at $N = 11$, beyond which the T-AA′ configuration becomes thermodynamically most stable.

Based on these theoretical results, the proposed bilayer growth scenario is illustrated in Figure 3d. Nucleation on top of the monolayer MoS_2 occurs with the assistance of a Mo interstitial, which reduces the activation barrier for nucleation. Initially, the structure adopts the O-AB′ stacking order due to the small nucleus size. As the second-layer grain grows, the top grain translates by breaking two bonds with the Mo interstitial, resulting in the T-AA′ configuration—consistent with atomic-resolution TEM observations (Figure 1e). Although the experimentally confirmed average size for a single interstitial ($N \sim 7$) is somewhat smaller than the theoretically predicted threshold ($N = 11$) required to stabilize the T-AA′ configuration, we hypothesize that additional Mo interstitials may be introduced following the formation of the AA′-stacked host. We note that the ΔE_{Moi} of at least 1.689 eV between different stacking orders is significantly higher than the ΔE_{Bulk} without interstitials (e.g., 1 meV per unit cell between hexagonal and rhombohedral phases; Figure S9). Therefore, the interstitials can strongly direct the formation of a specific stacking order at the nucleation stage. Furthermore, they can suppress the formation of strained solitons, which would require breaking the strong covalent bonds between the interstitial and the MoS_2 surface. Previous theoretical studies have proposed using Mo interstitials to control stacking orders for enhancing interlayer interactions and tuning the stacking-dependent formation energy of bilayer phases.[24,30,31] However, to the best of our knowledge, this represents the first experimental demonstration of the deterministic formation of a specific interstitial and its utilization to control the stacking order.

Structural and Chemical Properties of Bilayer MoS_2 with Mo Interstitials. We further compare the structural and chemical properties of bilayer MoS_2 with and without interstitials. In the Raman spectra (Figure 4a), the sample grown by MOCVD under Mo-poor conditions displays a single peak for the in-plane E^1_{2g} vibration mode, whereas the as-grown sample synthesized under Mo-rich conditions exhibits two clearly distinct peaks. This peak splitting persists after transferring the film from the growth substrate (Figure S10a), indicating that the splitting is not induced by substrate−film interactions. Similar peak splitting has been previously reported in bilayer MoS_2 containing covalently bonded Li interstitials.[32] We assign the peaks with lower and higher

https://doi.org/10.1021/acsnano.5c07577
ACS Nano XXXX, XXX, XXX−XXX

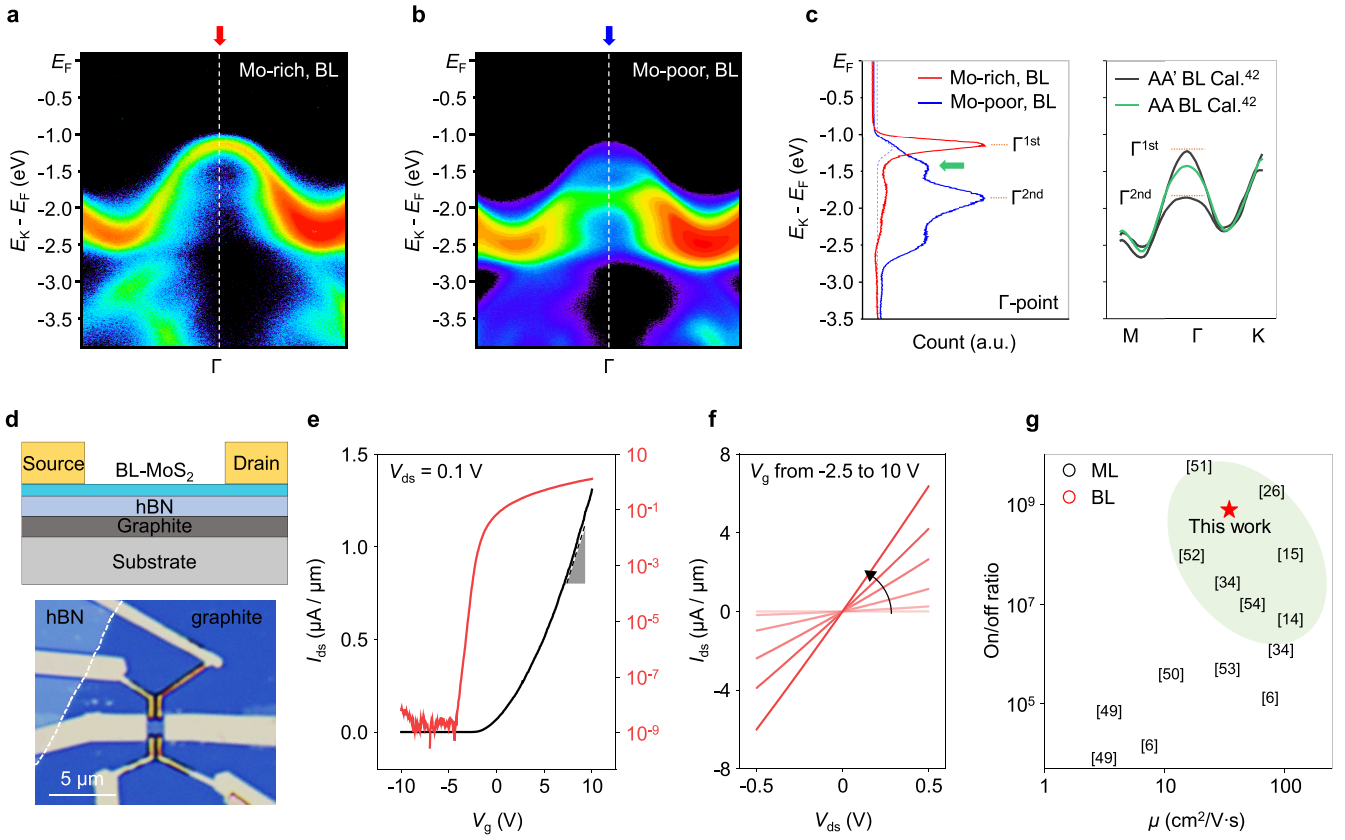

Figure 5. Band structure and electronic properties of bilayer MoS_2. (a), (b) Band dispersion of Γ direction obtained by ARPES which grown under Mo-rich and Mo-poor conditions, respectively. (c) Photoelectron intensity as a function of energy at the Γ point. Left: red and blue lines represent data from samples grown under Mo-rich and Mo-poor conditions, respectively. Right: calculated electronic band dispersions of 2H bilayer MoS_2 with AA′ (black) and AA (green) stacking orders, adapted from ref 42. (d) Schematic of the device structure (top) and optical microscopy image of the fabricated field-effect transistor (FET) device (bottom). Scale bar, 5 μm (L_{ch} = 1.35 μm, W_{ch} = 2.2 μm). (e) Transconductance curve (I_{ds} vs V_g) measured at V_{ds} = 0.1 V for bilayer MoS_2 grown under Mo-rich conditions. (f) Output characteristics (I_{ds} vs V_{ds}) of the same device shown in (e). V_g was varied from −2.5 to 10 V in 2.5 V steps. (g) Benchmark comparison of CVD-grown mono- and bilayer MoS_2 in terms of on/off ratio and field-effect mobility, compiled from references.[6,14,15,26,34,49−54]

Raman shifts to $E^1_{2g}(-)$ and $E^1_{2g}(+)$, respectively. The $E^1_{2g}(-)$ mode, which exhibits stronger intensity, is red-shifted by 5.7 cm^{-1} compared to the reported value for unstrained bilayer MoS_2.[33,34] Prior studies have shown that tensile strain can soften the E^1_{2g} phonon mode,[35,36] whereby the observed red-shift corresponds to a high tensile strain of approximately 1.6%. Such a high in-plane strain is unlikely to be maintained by weak vdW interactions with the substrate due to the intrinsic stiffness of the MoS_2 lattice. However, strong covalent bonding with interstitial atoms could plausibly induce and sustain this level of strain within the MoS_2 lattice.

X-ray photoelectron spectra (XPS) also reveal distinct differences between the two types of bilayer MoS_2. While peaks corresponding to Mo in the +4 oxidation state and S in the −2 oxidation state dominate both spectra,[37] the sample containing Mo interstitials exhibits symmetric broadening of the S 2p peak, resulting in an approximately 35% increase in the full width at half-maximum (Figure S10b). In contrast, the Mo 3d peak exhibits asymmetric broadening toward the lower binding energy, with additional shoulder peaks, attributed to Mo in lower oxidation states (red and blue highlighted peaks in Figure 4b). These extra peaks are shifted by approximately 1 eV to lower binding energy relative to the main Mo 3d peak, which is significantly larger than the typical shift of ∼ 0.5 eV associated with sulfur vacancies.[38] This observation supports our structural model of the bilayer with Mo interstitials, wherein excess Mo cations withdraw electrons from covalently bonded sulfur atoms, resulting in neighboring Mo atoms (highlighted as purple spheres in Figure 4c) being less oxidized. The fraction of less-oxidized Mo atoms is approximately 11.5% of the total Mo content (based on the Mo $3d_{5/2}$ in the XPS spectrum), which is consistent with the STEM results (∼11.3%).

We further note that the interstitials connecting adjacent layers to guide the stacking order exhibit identical atomic configurations, including their orientations. A Mo interstitial with tetrahedral bonding configuration can align with Mo atoms in either the bottom or top layer; however, TEM characterization (Figure 1e) shows that all observed interstitials align with Mo atoms in the bottom layer. The interstitial bonds, with a fixed out-of-plane polarity, are expected to be kinetically driven during layer-by-layer epitaxy. When the octahedral Mo configuration transitions to a tetrahedral one (Figure 3d), it is energetically favorable to slide the smaller top MoS_2 layer rather than the bottom layer by breaking the bonds between the Mo interstitial and the top layer.

Electronic Properties of Single-Crystalline Bilayer MoS_2. The robust stacking order and interstitial bonds with fixed bonding polarity result in uniform interlayer interactions across the sample. To investigate the electronic band structure,

https://doi.org/10.1021/acsnano.5c07577
ACS Nano XXXX, XXX, XXX−XXX

we performed angle-resolved photoemission spectroscopy (ARPES) on the bilayer MoS_2 samples. The ARPES measurement was conducted over a characterization area of approximately 300 × 150 μm^2, spanning a film region formed by the merging of multiple nuclei. Despite this, the bilayer MoS_2 grown under Mo-rich conditions exhibits single-crystalline band structures, as evidenced by the contour map of photoelectron intensity across momentum space at various binding energies (Figure S11a,b). The valence band dispersion along the high-symmetry Γ−K direction (Figure S11c) was extracted from the extrema of the photoelectron intensity (red line in Figure S11a) and aligns closely with previously reported data for a single crystal of hexagonal bilayer MoS_2 (dotted black line).[39]

The bilayer grown under Mo-poor conditions also exhibits characteristic features of a bilayer structure, with band extrema located at similar energy levels along the high-symmetry Γ−K−M path (Figure S11d). However, the intensity profiles at the Γ point, as a function of binding energy across the valence band maxima, reveal distinct differences between the two samples (Figure 5a,b). Theoretically, a bilayer crystal exhibits two distinct valence bands at the Γ point near the energy maximum,[40,41] denoted Γ^{first} and Γ^{second}, which are separated by approximately 0.71 eV. In the sample grown under Mo-rich conditions, the Γ^{first} valence band maximum appears as a clear intensity peak (Figure 5c, red plot). In contrast, the sample grown under Mo-poor conditions exhibits significantly weaker intensity at the Γ^{first} band (Figure 5c, blue plot). Additionally, the Mo-poor sample shows an extra spectral peak, indicated by a green arrow in Figure 5c, which does not correspond to any theoretically predicted band in either hexagonal AA' or rhombohedral AB/BA stacking configurations of stable bilayer MoS_2 (Figure 5c, right panel).[42]

The Γ^{first} band, associated with hybridized states between interfacing layers, strongly depends on out-of-plane interlayer interactions.[41−46] Efficient and uniform electronic coupling between layers in the Mo-rich sample likely accounts for the distinct peak at Γ^{first}. However, local regions with stacking faults—such as strained solitons abundantly observed in Figure 2h—may lead to weak hybridization of interlayer states, shifting the Γ^{first} band closer to the Γ^{second} and toward lower binding energy. Notably, the energy of the newly emerged band aligns with the theoretically predicted position of the Γ^{first} band in the thermodynamically unstable AA stacking configuration, which appears in regions of stacking faults, such as strained solitons, and exhibits weak interlayer interactions.[42,44]

We also investigate electronic transport across stacking-fault-free, single-crystalline bilayer MoS_2 in a field-effect transistor (FET). Atomically thin MoS_2 has gained attention as a channel material for low-power electronics.[2] While previously reported epitaxial growths of multilayer MoS_2 with aligned crystallinity[14] has shown enhanced carrier mobility by minimizing the carrier scattering at tilted grain boundaries, abundant stacking faults exist in the multilayers with conductive twin boundaries,[47] which can increase off-state currents. To characterize the intrinsic properties of the MoS_2 sample while minimizing external disorders,[48] single-crystalline hexagonal boron nitride (hBN) and graphite—exfoliated from bulk crystals—are employed as dielectric and gate materials, respectively. In the transconductance curve as a function of gate voltage (Figure 5e,f), the electron field-effect mobility is estimated to be approximately 35 $cm^2/V{\cdot}s$. Notably, the on/off ratio approaches 10^9, which is among the highest reported for multilayer MoS_2 channels (Figure 5g). The device also maintains stable electrical performance during extended operation (Figure S12). In a direct comparison of electrical properties between devices with the same geometry, FETs fabricated from bilayer MoS_2 channels grown under Mo-poor conditions exhibit significantly degraded performance (Figure S13). While various factors may contribute to this degradation, stacking variations within the channel are considered the primary factor determining the performance differences (see Figures S13 and S14 for discussion).

CONCLUSIONS

In summary, we present a method for synthesizing large-area, single-crystalline vdW multilayers that resist sliding or twisting under mechanical stress. By introducing single-atom interstitials at the interlayer during layer-by-layer epitaxy—under precisely controlled chemical environments in MOCVD—we enable the formation of dilute atomic anchors that connect layers in the thermodynamically most stable configuration. This approach guides stacking order with enhanced mechanical robustness and improved performance in electronic transport.

While the current study primarily focuses on the growth of bilayer MoS_2, the interstitial engineering strategy is applicable to multilayer systems beyond bilayers, where the chemical environment during growth is controlled to deterministically form specific types of atomic sites that guide the interlayer stacking order (Figures S15 and S16). Furthermore, this interstitial strategy for controlling stacking order can be extended to other TMDs with identical outer electron configurations of their constituent elements, supporting the general validity of the proposed growth mechanism (Figures 3 and S17). Finally, our strategy is adaptable to various vdW crystals incorporating different interstitial elements, enabling deterministic control of interlayer interactions and crystal symmetry.

METHODS

TMDs Growth. TMDs (MoS_2, WS_2) films were grown using a home-built MOCVD system. Sapphire substrates with a polished C-plane <0001> surface, miscut at 15° along the A-axis of <1120>, were used as epi-substrates. Before growth, the substrates were annealed at 1000 °C for 3 h in an Ar/H_2 atmosphere to induce surface reconstruction with atomic steps. During growth, NaCl and KCl powder were introduced near the furnace inlet to act as a growth promoter, respectively the case of MoS_2 and WS_2, facilitating precursor injection.

$Mo(CO)_6$ (Sigma-Aldrich 577766, ≥ 99.9%), $W(CO)_6$ (Sigma-Aldrich 472956, ≥ 99.9%), and $(C_2H_5)_2S$ (Sigma-Aldrich 107247, 98%) served as the Mo, W and S precursors, respectively. Each precursor was housed in a separate chamber, and their vapors were carried into the growth chamber using Ar as the carrier gas. Growth was conducted at 810 °C under a mixture of Ar and H_2 flows.

Under Mo-rich conditions, the flow rates for Ar, H_2, $(C_2H_5)_2S$ with Ar carrier gas and $Mo(CO)_6$ with Ar carrier gas were 500, 2, 0.1, and 2.0 sccm, respectively. For Mo-poor conditions, the corresponding flow rates were 90, 4, 0.4, and 0.4 sccm. The partial pressures of the Mo and S precursors in the growth chamber, P_{Mo} and P_S, were estimated based on the vapor pressures in their respective precursor chambers and the carrier gas flow rates. For the Mo-rich condition, $P_{Mo} = 8.5 \times 10^{-5}$ Torr and $P_S = 2.1 \times 10^{-3}$ Torr; for the Mo-poor condition, $P_{Mo} = 1.7 \times 10^{-5}$ Torr, $P_S = 8.6 \times 10^{-3}$ Torr.

Under W-rich conditions, the flow rates for Ar, H_2, $(C_2H_5)_2S$ with Ar carrier gas and $W(CO)_6$ with Ar carrier gas were 700, 2.5, 0.1, and 3.0 sccm, respectively. For W-poor conditions, the corresponding flow

https://doi.org/10.1021/acsnano.5c07577
ACS Nano XXXX, XXX, XXX−XXX

rates were 80, 0, 0.2, and 0.3 sccm. The partial pressures of the W and S precursors in the growth chamber, P_W and P_S, were estimated based on the vapor pressures in their respective precursor chambers and the carrier gas flow rates. For the W-rich condition, $P_W = 8.6 \times 10^{-5}$ Torr and $P_S = 2.1 \times 10^{-3}$ Torr; for the W-poor condition, $P_W = 8.6 \times 10^{-6}$ Torr, $P_S = 4.2 \times 10^{-3}$ Torr.

DFT Calculations. DFT calculations were performed as implemented in the Vienna *ab initio* simulation package (VASP) code.[55] The projector-augmented wave (PAW) pseudopotentials[56,57] and a kinetic energy cutoff of 500 eV were applied. The Perdew, Burke, and Ernzerhof (PBE) functional within the generalized gradient approximation (GGA) was used for the exchange correlation functional,[58] and the vdW-D3 correction proposed by Grimme was used to describe the long-range vdW interaction.[59] Spin-polarization was included. The calculated hexagonal lattice constant of bulk MoS_2 was 3.161 Å. The in-plane 6 × 6 and out-of-plane 4-MoS_2-layer-thick supercell of MoS_2 was used, and the Γ, *K*-point was used for the Brillouin zone summation. The local atomic configurations were relaxed to less than 0.001 eV/Å in the Hellmann−Feynman forces. In calculations of formation energies, the total energies of a Mo bcc metal and a S orthorhombic crystal were chosen for the Mo- and S-rich limits, respectively.

TEM Characterizations. For DF-TEM imaging from selected diffraction spots with the objective filtering aperture, MoS_2, WS_2 samples were transferred onto a 20 nm thick silicon nitride membrane, then imaging was conducted using a JEOL JEM-2100F operated at 200 kV.

For STEM imaging, samples were transferred onto a Quantifoil TEM Cu-grid. The STEM data were obtained using a JEOL JEM-ARM 200F equipped with a fifth-order spherical aberration corrector (ASCOR, CEOS GMBH) at the Materials Imaging & Analysis Center of POSTECH in South Korea. The acceleration voltage was set to 80 kV, and a high-angle annular dark-field detector (inner angle: 54 mrad, outer angle: 216 mrad) with 40-μm condenser lens aperture was used to acquire the STEM images.

ARPES Measurements. ARPES measurements were conducted at the 10D beamline of the Pohang Accelerator Laboratory (PAL) using a Scienta DA30 analyzer under ultrahigh vacuum (~10^{-9} Torr) at room temperature, with a photon energy of 56 eV. Samples were prepared by depositing an 80 nm thick Au layer onto the as-grown MoS_2, serving as a transfer medium. The Au-coated surface was mounted onto the sample holder and secured with Ta foil. In the load-lock chamber, once ultrahigh vacuum was achieved, the sapphire substrate was detached from the MoS_2 to avoid contamination prior to measurement. The Fermi level was calibrated using an Au reference.

Device Fabrication and Transport Measurements. For back-gated field-effect transistors (FETs) with an hBN dielectric (Figures 5d and S12), graphite (~10 nm thick) and hBN (30 nm thick) were sequentially exfoliated from bulk crystals and transferred onto a Si/SiO_2 substrate. The as-grown MoS_2 was then transferred onto the graphite/hBN stack using a PMMA superlayer. Electron-beam lithography was employed to define the electrode and channel regions, followed by deposition of Bi/Au (15:45 nm) to form source and drain contacts and Ti/Au (5:40 nm) was deposited on the pad region.

For back-gated FETs with an Al_2O_3 dielectric (Figure S13), Cr/Au (10:40 nm) was first deposited on a Si/SiO_2 substrate. A 30 nm thick Al_2O_3 layer was subsequently deposited via atomic layer deposition (Plus 200, QUROS). The MoS_2 film was transferred onto the Al_2O_3 surface, and device geometry was defined using photolithography. Source and drain contacts were formed with Bi/Au (15:45 nm), and MoS_2 channels were patterned using oxygen-reactive ion etching. Electrical measurements were conducted under vacuum (~10^{-5} Torr) at room temperature.

Other Characterizations. Raman and photoluminescence spectroscopy were performed at room temperature using a 532 nm laser (power: 10−30 mW), focused onto the sample through a 100× microscope objective lens (0.9 N.A.). The spectrometer was configured with a grating of 1800 grooves/mm.

X-ray photoelectron spectroscopy (XPS) was carried out using a Thermo Fisher Scientific system equipped with an Al K-alpha X-ray source ($h\nu$ = 1486.6 eV, 15 kV, 100 W), producing a spot size of 400 μm in diameter. Charge compensation was applied using dual flood guns (low-energy electrons and Ar^+ ions).

ASSOCIATED CONTENT

Supporting Information

The Supporting Information is available free of charge at https://pubs.acs.org/doi/10.1021/acsnano.5c07577.

Epitaxial growth of monolayer MoS_2, atomic-resolution images and phase distribution analysis of bilayer MoS_2 grown under Mo-rich and Mo-poor conditions, calculated formation energies of bilayer MoS_2 structures containing Mo interstitials, Raman and X-ray photoelectron spectroscopy results of bilayer MoS_2, electronic band dispersions of bilayer MoS_2, electronic transport characteristics of bilayer MoS_2, stacking order analysis in trilayer MoS_2, and transmission electron microscopy analysis of bilayer WS2 grown under W-rich conditions (PDF)

AUTHOR INFORMATION

Corresponding Authors

Yong-Sung Kim − *Korea Research Institute of Standards and Science (KRISS), Daejeon 34113, Republic of Korea;* orcid.org/0000-0002-6057-2997; Email: yongsung.kim@kriss.re.kr

Si-Young Choi − *Center for Epitaxial van der Waals Quantum Solids, Institute for Basic Science (IBS), Pohang 37673, Republic of Korea; Department of Materials Science & Engineering and Department of Semiconductor Engineering, POSTECH, Pohang 37673, Republic of Korea;* orcid.org/0000-0003-1648-142X; Email: youngchoi@postech.ac.kr

Moon-Ho Jo − *Center for Epitaxial van der Waals Quantum Solids, Institute for Basic Science (IBS), Pohang 37673, Republic of Korea; Department of Materials Science & Engineering, POSTECH, Pohang 37673, Republic of Korea;* orcid.org/0000-0002-3160-358X; Email: mhjo@postech.ac.kr

Cheol-Joo Kim − *Center for Epitaxial van der Waals Quantum Solids, Institute for Basic Science (IBS), Pohang 37673, Republic of Korea; Department of Chemical Engineering, Pohang University of Science and Technology (POSTECH), Pohang 37673, Republic of Korea;* orcid.org/0000-0002-4312-3866; Email: kimcj@postech.ac.kr

Authors

GunWoo Yoo − *Center for Epitaxial van der Waals Quantum Solids, Institute for Basic Science (IBS), Pohang 37673, Republic of Korea; Department of Chemical Engineering, Pohang University of Science and Technology (POSTECH), Pohang 37673, Republic of Korea*

TaeJoon Mo − *Center for Epitaxial van der Waals Quantum Solids, Institute for Basic Science (IBS), Pohang 37673, Republic of Korea; Department of Chemical Engineering, Pohang University of Science and Technology (POSTECH), Pohang 37673, Republic of Korea*

Chang-Won Choi − *Center for Epitaxial van der Waals Quantum Solids, Institute for Basic Science (IBS), Pohang 37673, Republic of Korea; Department of Materials Science*

https://doi.org/10.1021/acsnano.5c07577
ACS Nano XXXX, XXX, XXX−XXX

& Engineering, POSTECH, Pohang 37673, Republic of Korea; orcid.org/0000-0003-3620-7460

Gunho Moon − *Center for Epitaxial van der Waals Quantum Solids, Institute for Basic Science (IBS), Pohang 37673, Republic of Korea; Department of Materials Science & Engineering, POSTECH, Pohang 37673, Republic of Korea*

Sumin Lee − *Center for Epitaxial van der Waals Quantum Solids, Institute for Basic Science (IBS), Pohang 37673, Republic of Korea; Department of Materials Science & Engineering, POSTECH, Pohang 37673, Republic of Korea*

Chan-Cuk Hwang − *Beamline Research Division, Pohang Accelerator Laboratory, Pohang 37673, Republic of Korea*

Woo-Ju Lee − *Center for Epitaxial van der Waals Quantum Solids, Institute for Basic Science (IBS), Pohang 37673, Republic of Korea; Department of Chemical Engineering, Pohang University of Science and Technology (POSTECH), Pohang 37673, Republic of Korea*

Min-Yeong Choi − *Center for Epitaxial van der Waals Quantum Solids, Institute for Basic Science (IBS), Pohang 37673, Republic of Korea; Department of Chemical Engineering, Pohang University of Science and Technology (POSTECH), Pohang 37673, Republic of Korea;* orcid.org/0000-0001-6966-3513

Jongyun Choi − *Center for Epitaxial van der Waals Quantum Solids, Institute for Basic Science (IBS), Pohang 37673, Republic of Korea; Department of Materials Science & Engineering, POSTECH, Pohang 37673, Republic of Korea*

Complete contact information is available at: https://pubs.acs.org/10.1021/acsnano.5c07577

Author Contributions

[V]G.W.Y. and T.J.M. contributed equally to this work. G.W.Y., T.J.M., M.-H.J., and C.-J.K.: Designed the project. G.W.Y., W.-J.L., and M.-Y.C.: Built MOCVD systems. G.W.Y. and T.J.M.: Synthesized MoS_2 samples. Y.-S.K.: Performed the DFT calculations. C.-W.C. and S.-Y.C.: Performed the STEM imaging and analysis. G.W.Y., G.H.M., S.M.L., and J.Y.C.: Fabricated the devices and conducted transport measurements. G.W.Y., T.J.M., and W.-J.L.: Performed ARPES measurements and C.-C.H.: Assisted to analyze the ARPES measurement data. G.W.Y., T.J.M., and C.-J.K.: Wrote the manuscript with inputs from all authors.

Funding

This research was supported by the National R&D Program through the National Research Foundation of Korea (NRF) funded by the Ministry of Science and ICT (2023R1A2C2005427, RS-2023−00258309), and the Institute for Basic Science (IBS-R034-D1).

Notes

The authors declare no competing financial interest.

REFERENCES

(1) Zheng, F.; Meng, W.; Li, L. J. Continue the Scaling of Electronic Devices with Transition Metal Dichalcogenide Semiconductors. *Nano Lett.* **2025**, *25* (10), 3683−3691.

(2) Liu, Y.; Duan, X.; Shin, H. J.; Park, S.; Huang, Y.; Duan, X. Promises and prospects of two-dimensional transistors. *Nature* **2021**, *591* (7848), 43−53.

(3) Lieth, R. M. A. *Preparation and Crystal Growth of Materials with Layered Structures*; Springer Science & Business Media, 1977; Vol. *1*.

(4) Manzeli, S.; Ovchinnikov, D.; Pasquier, D.; Yazyev, O. V.; Kis, A. 2D transition metal dichalcogenides. *Nat. Rev. Mater.* **2017**, *2* (8), No. 17033.

(5) Zeng, Z.; Sun, X.; Zhang, D.; Zheng, W.; Fan, X.; He, M.; Xu, T.; Sun, L.; Wang, X.; Pan, A. Controlled vapor growth and nonlinear optical applications of large-area 3R phase WS_2 and WSe_2 atomic layers. *Adv. Funct. Mater.* **2019**, *29* (11), No. 1806874.

(6) Zhang, X.; Nan, H.; Xiao, S.; Wan, X.; Gu, X.; Du, A.; Ni, Z.; Ostrikov, K. Transition metal dichalcogenides bilayer single crystals by reverse-flow chemical vapor epitaxy. *Nat. Commun.* **2019**, *10* (1), No. 598.

(7) Peng, G.; Yang, X.; Wang, S.; Zhang, J.; Qi, G.; Zhang, S.; Liu, K.; Zhu, Z. H.; Li, Z.; Wang, G.; Zhu, M.; Qin, S. Controllable epitaxial growth of $MoSe_2$ bilayers with different stacking orders by reverse-flow chemical vapor deposition. *ACS Appl. Mater. Interfaces* **2020**, *12* (20), 23347−23355.

(8) Ma, T.; Chen, H.; Yananose, K.; Zhou, X.; Wang, L.; Li, R.; Zhu, Z.; Wu, Z.; Xu, Q.-H.; Yu, J.; Qiu, W. C.; Stroppa, A.; Loh, K. P. Growth of bilayer $MoTe_2$ single crystals with strong non-linear Hall effect. *Nat. Commun.* **2022**, *13* (1), No. 5465.

(9) Song, S.; Keum, D. H.; Cho, S.; Perello, D.; Kim, Y.; Lee, Y. H. Room temperature semiconductor−metal transition of $MoTe_2$ thin films engineered by strain. *Nano Lett.* **2016**, *16* (1), 188−193.

(10) Awate, S. S.; Xu, K.; Liang, J.; Katz, B.; Muzzio, R.; Crespi, V. H.; Katoch, J.; Fullerton-Shirey, S. K. Strain-induced 2H to 1T′ phase transition in suspended $MoTe_2$ using electric double layer gating. *ACS Nano* **2023**, *17* (22), 22388−22398.

(11) Liu, L.; Wu, J.; Wu, L.; Ye, M.; Liu, X.; Wang, Q.; Hou, S.; Lu, P.; Sun, L.; Zheng, J.; Xing, L.; Gu, L.; Jiang, Z.; Xie, L.; Jiao, L. Phase-selective synthesis of 1T′ MoS_2 monolayers and heterophase bilayers. *Nat. Mater.* **2018**, *17* (12), 1108−1114.

(12) Zhao, X.; Song, P.; Wang, C.; Riis-Jensen, A. C.; Fu, W.; Deng, Y.; Wan, D.; Kang, L.; Ning, S.; Dan, J.; Venkatesan, T.; Liu, Z.; Zhou, W.; Thygesen, K. S.; Luo, X.; Pennycook, S. J.; Loh, K. P. Engineering covalently bonded 2D layered materials by self-intercalation. *Nature* **2020**, *581* (7807), 171−177.

(13) Kappera, R.; Voiry, D.; Yalcin, S. E.; Branch, B.; Gupta, G.; Mohite, A. D.; Chhowalla, M. Phase-engineered low-resistance contacts for ultrathin MoS_2 transistors. *Nat. Mater.* **2014**, *13* (12), 1128−1134.

(14) Liu, L.; Li, T.; Ma, L.; Li, W.; Gao, S.; Sun, W.; Dong, R.; Zou, X.; Fan, D.; Shao, L.; Gu, C.; Dai, N.; Yu, Z.; Chen, X.; Tu, X.; Nie, Y.; Wang, P.; Wang, J.; Shi, Y.; Wang, X. Uniform nucleation and epitaxy of bilayer molybdenum disulfide on sapphire. *Nature* **2022**, *605* (7908), 69−75.

(15) Wang, Q.; Tang, J.; Li, X.; Tian, J.; Liang, J.; Li, N.; Ji, D.; Xian, L.; Guo, Y.; Li, L.; Zhang, Q.; Chu, Y.; Wei, Z.; Zhao, Y.; Du, L.; Yu, H.; Bai, X.; Gu, L.; Liu, K.; Zhang, G.; et al. Layer-by-layer epitaxy of multi-layer MoS_2 wafers. *Natl. Sci. Rev.* **2022**, *9* (6), No. nwac077, DOI: 10.1093/nsr/nwac077.

(16) Zhang, X.; Nan, H.; Xiao, S.; Wan, X.; Gu, X.; Du, A.; Ni, Z.; Ostrikov, K. Transition metal dichalcogenides bilayer single crystals by reverse-flow chemical vapor epitaxy. *Nat. Commun.* **2019**, *10* (1), No. 598.

(17) Chang, C.; Zhang, X.; Li, W.; Guo, Q.; Feng, Z.; Huang, C.; Ren, Y.; Cai, Y.; Zhou, X.; Wang, J.; Tang, Z.; Ding, F.; Wei, W.; Liu, K.; Xu, X. Remote epitaxy of single-crystal rhombohedral WS_2 bilayers. *Nat. Commun.* **2024**, *15* (1), No. 4130.

(18) Qin, B.; Ma, C.; Guo, Q.; Li, X.; Wei, W.; Ma, C.; Wang, Q.; Liu, F.; Zhao, M.; Xue, G.; Qi, J.; Wu, M.; Hong, H.; Du, L.; Zhao, Q.; Gao, P.; Wang, E.; Wang, E.; Zhang, G.; Liu, C.; Liu, K. Interfacial epitaxy of multilayer rhombohedral transition-metal dichalcogenide single crystals. *Science* **2024**, *385* (6704), 99−104.

(19) Weston, A.; Castanon, E. G.; Enaldiev, V.; Ferreira, F.; Bhattacharjee, S.; Xu, S.; Corte-León, H.; Wu, Z.; Clark, N.; Summerfield, A.; Hashimoto, T.; Gao, Y.; Wang, W.; Hamer, M.; Read, H.; Fumagalli, L.; Kretinin, A. V.; Haigh, S. J.; Kazakova, O.; Gorbachev, R.; et al. Interfacial ferroelectricity in marginally twisted 2D semiconductors. *Nat. Nanotechnol.* **2022**, *17* (4), 390−395.

(20) Ko, K.; Yuk, A.; Engelke, R.; Carr, S.; Kim, J.; Park, D.; Heo, H.; Kim, H.-M.; Kim, S.-G.; Kim, H.; Taniguchi, T.; Watanabe, K.; Park, H.; Kaxiras, E.; Yang, S. M.; Kim, P.; Yoo, H. Operando electron

microscopy investigation of polar domain dynamics in twisted van der Waals homobilayers. *Nat. Mater.* **2023**, *22* (8), 992−998.
(21) Kim, C.-J.; Brown, L.; Graham, M. W.; Hovden, R.; Havener, R. W.; McEuen, P. L.; Muller, D. A.; Park, J. Stacking Order Dependent Second Harmonic Generation and Topological Defects in h-BN Bilayers. *Nano Lett.* **2013**, *13* (11), 5660−5665.
(22) Kim, J. H.; Kim, S. Y.; Cho, Y.; Park, H. J.; Shin, H. J.; Kwon, S. Y.; Lee, Z. Interface-driven partial dislocation formation in 2D heterostructures. *Adv. Mater.* **2019**, *31* (15), No. 1807486.
(23) Alden, J. S.; Tsen, A. W.; Huang, P. Y.; Hovden, R.; Brown, L.; Park, J.; Muller, D.; McEuen, P. L. Strain solitons and topological defects in bilayer graphene. *Proc. Natl. Acad. Sci. U.S.A.* **2013**, *110* (28), 11256−11260.
(24) Cortés, N.; Rosales, L.; Orellana, P. A.; Ayuela, A.; González, J. W. Stacking change in MoS_2 bilayers induced by interstitial Mo impurities. *Sci. Rep.* **2018**, *8* (1), No. 2143.
(25) Zhang, P.; Xue, M.; Chen, C.; Guo, W.; Zhang, Z. Mechanism regulating self-intercalation in layered materials. *Nano Lett.* **2023**, *23* (8), 3623−3629.
(26) Li, T.; Guo, W.; Ma, L.; Li, W.; Yu, Z.; Han, Z.; Gao, S.; Liu, L.; Fan, D.; Wang, Z.; Yang, Y.; Lin, W.; Luo, Z.; Chen, X.; Dai, N.; Tu, X.; Pan, D.; Yao, Y.; Wang, P.; Wang, X.; et al. Epitaxial growth of wafer-scale molybdenum disulfide semiconductor single crystals on sapphire. *Nat. Nanotechnol.* **2021**, *16* (11), 1201−1207.
(27) Hensling, F. V. E.; Braun, W.; Kim, D. Y.; Majer, L. N.; Smink, S.; Faeth, B. D.; Mannhart, J. State of the art, trends, and opportunities for oxide epitaxy. *APL Mater.* **2024**, *12* (4), No. 040902.
(28) Brown, L.; Hovden, R.; Huang, P.; Wojcik, M.; Muller, D. A.; Park, J. Twinning and twisting of tri-and bilayer graphene. *Nano Lett.* **2012**, *12* (3), 1609−1615.
(29) Zeng, Z.; Sun, X.; Zhang, D.; Zheng, W.; Fan, X.; He, M.; Xu, T.; Sun, L.; Wang, X.; Pan, A. Controlled vapor growth and nonlinear optical applications of large-area 3R phase WS_2 and WSe_2 atomic layers. *Adv. Funct. Mater.* **2019**, *29* (11), No. 1806874.
(30) Zhang, F.; Wang, Y.; Erb, C.; Wang, K.; Moradifar, P.; Crespi, V. H.; Alem, N. Full orientation control of epitaxial MoS_2 on hBN assisted by substrate defects. *Phys. Rev. B* **2019**, *99* (15), No. 155430.
(31) Huang, Z.; Hao, G.; He, C.; Yang, H.; Xue, L.; Qi, X.; Peng, X.; Zhong, J. Density functional theory study of Fe adatoms adsorbed monolayer and bilayer MoS_2 sheets. *J. Appl. Phys.* **2013**, *114* (8), No. 083706.
(32) Wu, Y.; Wang, J.; Li, Y.; Zhou, J.; Wang, B. Y.; Yang, A.; Wang, W.; Hwang, H.; Cui, Y. Observation of an intermediate state during lithium intercalation of twisted bilayer MoS_2. *Nat. Commun.* **2022**, *13* (1), No. 3008.
(33) Li, H.; Zhang, Q.; Yap, C. C. R.; Tay, B. K.; Edwin, T. H. T.; Olivier, A.; Baillargeat, D. From bulk to monolayer MoS_2: evolution of Raman scattering. *Adv. Funct. Mater.* **2012**, *22* (7), 1385−1390.
(34) Kim, T. S.; Noh, G.; Kwon, S.; Kim, J. Y.; Dhakal, K. P.; Oh, S.; Chai, H.-J.; Park, E.; Kim, I. S.; Lee, E.; Kim, Y.; Lee, J.; Jo, M.-K.; Kang, M.; Park, C.; Kim, J.; Park, J.; Kim, S.; Kim, M.; Kang, K.; et al. Diffusion Control on the Van der Waals Surface of Monolayers for Uniform Bi-Layer MoS_2 Growth. *Adv. Funct. Mater.* **2024**, *34* (23), No. 2312365.
(35) Lee, J. U.; Woo, S.; Park, J.; Park, H. C.; Son, Y. W.; Cheong, H. Strain-shear coupling in bilayer MoS_2. *Nat. Commun.* **2017**, *8* (1), No. 1370.
(36) Conley, H. J.; Wang, B.; Ziegler, J. I.; Haglund, R. F., Jr; Pantelides, S. T.; Bolotin, K. I. Bandgap engineering of strained monolayer and bilayer MoS_2. *Nano Lett.* **2013**, *13* (8), 3626−3630.
(37) Chastain, J.; King, R. C., Jr *Handbook of X-ray Photoelectron Spectroscopy*; Perkin-Elmer Corporation, 1992.
(38) Pierucci, D.; Henck, H.; Aziza, Z. B.; Naylor, C. H.; Balan, A.; Rault, J. E.; Silly, M. G.; Dappe, Y. J.; Bertran, F.; Le Fèvre, P.; Sirotti, F.; Johnson, A. T. C.; Ouerghi, A. Tunable Doping in Hydrogenated Single Layered Molybdenum Disulfide. *ACS Nano* **2017**, *11* (2), 1755−1761.
(39) Jin, W.; Yeh, P.-C.; Zaki, N.; Zhang, D.; Sadowski, J. T.; Al-Mahboob, A.; van der Zande, A. M.; Chenet, D. A.; Dadap, J. I.; Herman, I. P.; Sutter, P.; Hone, J.; Osgood, R. M. Direct Measurement of the Thickness-Dependent Electronic Band Structure of MoS_2 Using Angle-Resolved Photoemission Spectroscopy. *Phys. Rev. Lett.* **2013**, *111* (10), No. 106801.
(40) Liu, K.; Zhang, L.; Cao, T.; Jin, C.; Qiu, D.; Zhou, Q.; Zettl, A.; Yang, P.; Louie, S. G.; Wang, F. Evolution of interlayer coupling in twisted molybdenum disulfide bilayers. *Nat. Commun.* **2014**, *5* (1), No. 4966.
(41) Wilson, N. R.; Nguyen, P. V.; Seyler, K.; Rivera, P.; Marsden, A. J.; Laker, Z. P.; Constantinescu, G. C.; Kandyba, V.; Barinov, A.; Hine, N.; Xu, X.; Cobden, D. H. Determination of band offsets, hybridization, and exciton binding in 2D semiconductor heterostructures. *Sci. Adv.* **2017**, *3* (2), No. e1601832.
(42) He, J.; Hummer, K.; Franchini, C. Stacking effects on the electronic and optical properties of bilayer transition metal dichalcogenides MoS_2, $MoSe_2$, WS_2, and WSe_2. *Phys. Rev. B* **2014**, *89* (7), No. 075409.
(43) Trainer, D. J.; Putilov, A. V.; Di Giorgio, C.; Saari, T.; Wang, B.; Wolak, M.; Chandrasena, R. U.; Lane, C.; Chang, T.-R.; Jeng, H.-T.; Lin, H.; Kronast, F.; Gray, A. X.; Xi, X.; Nieminen, J.; Bansil, A.; Iavarone, M. Inter-Layer Coupling Induced Valence Band Edge Shift in Mono- to Few-Layer MoS_2. *Sci. Rep.* **2017**, *7* (1), No. 40559.
(44) Yeh, P.-C.; Jin, W.; Zaki, N.; Kunstmann, J.; Chenet, D.; Arefe, G.; Sadowski, J. T.; Dadap, J. I.; Sutter, P.; Hone, J.; Osgood, R. M., Jr. Direct Measurement of the Tunable Electronic Structure of Bilayer MoS_2 by Interlayer Twist. *Nano Lett.* **2016**, *16* (2), 953−959.
(45) Kinoshita, K.; Moriya, R.; Okazaki, S.; Onodera, M.; Zhang, Y.; Watanabe, K.; Taniguchi, T.; Sasagawa, T.; Machida, T. Control of Subband Energies via Interlayer Twisting in an Artificially Stacked WSe_2 Bilayer. *Nano Lett.* **2024**, *24* (39), 12211−12217.
(46) Arnold, F. M.; Ghasemifard, A.; Kuc, A.; Heine, T. Implementing electronic signatures of graphene and hexagonal boron nitride in twisted bilayer molybdenum disulfide. *Mater. Today* **2024**, *73*, 96−104.
(47) Ahn, H.; Moon, G.; Jung, H.-G.; Deng, B.; Yang, D.-H.; Yang, S.; Han, C.; Cho, H.; Yeo, Y.; Kim, C.-J.; Yang, C.-H.; Kim, J.; Choi, S.-Y.; Park, H.; Jeon, J.; Park, J.-H.; Jo, M.-H. Integrated 1D epitaxial mirror twin boundaries for ultrascaled 2D MoS_2 field-effect transistors. *Nat. Nanotechnol.* **2024**, *19* (7), 955−961.
(48) Illarionov, Y. Y.; Knobloch, T.; Jech, M.; Lanza, M.; Akinwande, D.; Vexler, M. I.; Mueller, T.; Lemme, M. C.; Fiori, G.; Schwierz, F.; Grasser, T. Insulators for 2D nanoelectronics: the gap to bridge. *Nat. Commun.* **2020**, *11* (1), No. 3385.
(49) Yan, D.; Ding, B.; Wang, L.; Li, L.; Ren, X.; Li, J.; Fang, Q.; Cao, D.; Zhang, G.; Xia, C.; Song, Q. Preparation and properties of bilayer MoS_2 with different stacking structures. *Appl. Surf. Sci.* **2025**, *695*, No. 162875.
(50) Yang, P.; Zhang, S.; Pan, S.; Tang, B.; Liang, Y.; Zhao, X.; Zhang, Z.; Shi, J.; Huan, Y.; Shi, Y.; Pennycook, S. J.; Ren, Z.; Zhang, G.; Chen, Q.; Zou, X.; Liu, Z.; Zhang, Y. Epitaxial growth of centimeter-scale single-crystal MoS_2 monolayer on Au (111). *ACS Nano* **2020**, *14* (4), 5036−5045.
(51) Mondal, A.; Biswas, C.; Park, S.; Cha, W.; Kang, S. H.; Yoon, M.; Choi, S. H.; Kim, K. K.; Lee, Y. H. Low Ohmic contact resistance and high on/off ratio in transition metal dichalcogenides field-effect transistors via residue-free transfer. *Nat. Nanotechnol.* **2024**, *19* (1), 34−43.
(52) Kandybka, I.; Groven, B.; Silva, H. M.; Sergeant, S.; Mehta, A. N.; Koylan, A.; Shi, S.; Banerjee, Y.; Morin, S.; Delabie, P. A. Chemical vapor deposition of a single-crystalline MoS_2 monolayer through anisotropic 2D crystal growth on stepped sapphire surface. *ACS Nano* **2024**, *18* (4), 3173−3186.
(53) McClellan, C. J.; Yalon, E.; Smithe, K. K.; Suryavanshi, S. V.; Pop, E. High current density in monolayer MoS_2 doped by AlO_x. *ACS Nano* **2021**, *15* (1), 1587−1596.
(54) Yu, H.; Huang, L.; Zhou, L.; Peng, Y.; Li, X.; Yin, P.; Zhao, J.; Zhu, M.; Wang, S.; Liu, J.; Du, H.; Tang, J.; Zhang, S.; Zhou, Y.; Lu, N.; Liu, K.; Li, N.; Zhang, G. Eight In. Wafer-Scale Epitaxial Monolayer MoS_2. *Adv. Mater.* **2024**, *36* (30), No. 2402855.

https://doi.org/10.1021/acsnano.5c07577
ACS Nano XXXX, XXX, XXX−XXX

(55) Kresse, G.; Furthmüller, J. Efficient iterative schemes for ab initio total-energy calculations using a plane-wave basis set. *Phys. Rev. B* **1996**, *54* (16), No. 11169.
(56) Blöchl, P. E. Projector augmented-wave method. *Phys. Rev. B* **1994**, *50* (24), No. 17953.
(57) Kresse, G.; Joubert, D. From ultrasoft pseudopotentials to the projector augmented-wave method. *Phys. Rev. B* **1999**, *59* (3), No. 1758.
(58) Perdew, J. P.; Burke, K.; Ernzerhof, M. Generalized gradient approximation made simple. *Phys. Rev. Lett.* **1996**, *77* (18), No. 3865.
(59) Ehrlich, S.; Moellmann, J.; Grimme, S. Dispersion-corrected density functional theory for aromatic interactions in complex systems. *Acc. Chem. Res.* **2013**, *46* (4), 916−926.

https://doi.org/10.1021/acsnano.5c07577
ACS Nano XXXX, XXX, XXX−XXX